RSC Advances

PAPER

View Article Online
View Journal | View Issue

Cite this: *RSC Adv.*, 2026, **16**, 3192

g-C_3N_4/CoN_4 heterojunction as a sensor for detecting volatile organic compounds: a density functional study

V. N. Dhilshada, M. Shilpa and Mausumi Chattopadhyaya *

Utilizing density functional theory (DFT) calculations, we investigated the adsorption behavior of key exhaled breath biomarkers – benzene, toluene, aniline, and *o*-toluidine – on both pristine g-C_3N_4 and g-C_3N_4/CoN_4 composite surfaces. By analyzing the key parameters such as adsorption energy, electronic density of states (DOS), band structures, charge density difference, conductivity and work function we gained critical insight into the interaction mechanisms between the gas molecules and the sensor surfaces. Our results reveal that the incorporation of CoN_4 significantly enhances the chemical reactivity and stability of the g-C_3N_4 substrate, further improving upon gas adsorption. Notably, benzene, toluene, and aniline exhibit reversible adsorption behavior on g-C_3N_4/CoN_4, highlighting their suitability for reusable gas sensor applications. In contrast, *o*-toluidine shows irreversible binding, potentially limiting its reusability. Aniline exhibits the lowest band gap and highest conductivity, highest sensitivity and strongest orbital hybridization, confirming that the g-C_3N_4/CoN_4 substrate acts as the best sensor towards aniline gas molecules, among the investigated molecules. Band structure analysis of aniline adsorbed on the g-C_3N_4/CoN_4 heterostructure further confirms that the composite exhibits improved electrical conductivity, even at room temperature, reinforcing its potential for biomarker sensing in human breath analysis. These theoretical findings establish g-C_3N_4/CoN_4 as a promising candidate material and provide predictive guidelines for future experimental investigations into selective and sensitive detection of benzene-related VOCs.

Received 13th June 2025
Accepted 23rd December 2025

DOI: 10.1039/d5ra04202j

rsc.li/rsc-advances

1 Introduction

Lung cancer is a major global health issue, ranking second in terms of prevalence and a leading cause of cancer-related deaths worldwide.[1] Despite significant strides in diagnostic techniques, therapeutic approaches, and modern medication, the overall success rate in curing lung cancer remains unsatisfactory. However, early detection through screening programs for high-risk individuals can substantially enhance survival rates by enabling diagnosis at earlier stages of the disease.[1]

Changes in bioelectric signals have been associated with various cancers, including those affecting the breast, lung, liver, brain, pancreas, and prostate.[2] These bioelectric alterations could potentially serve as early indicators for cancer detection. Moreover, each type of cancer is linked to specific metabolic and biochemical processes, resulting in the production of unique volatile organic compound (VOC) profiles. These distinct VOC patterns, associated with different cancers and affected organs, can be used to differentiate between healthy individuals and those with cancer, as well as to identify the specific type of cancer.[2] Detecting these biomarkers from exhaled breath samples offers a simple, affordable, and non-invasive method, potentially playing a crucial role in the early detection of lung cancer.[3]

Among the reported exhaled VOCs, benzene, aniline, toluene, and *o*-toluidine are recognized as important lung cancer biomarkers. These compounds have been frequently detected in breath samples of lung cancer patients and, even at trace concentrations, provide valuable diagnostic information. Hence, the development of highly sensitive and selective sensing platforms for their detection is of great clinical significance. In this context, Gregis *et al.*[4] found that activated carbon microspheres (W_5) and zeolite NaY are the most effective materials for adsorbing toluene gas at very low concentrations. Ayad *et al.*[5] developed a sensor using the quartz crystal microbalance (QCM) technique to detect various primary aliphatic alcohols, including ethanol, methanol, 1-propanol, and 2-propanol vapors. The detection mechanism relies on a thin, sensitive polyaniline film coated onto the QCM electrode, enabling effective identification of these alcohol vapors. Luo *et al.*[6] reported that Co-doped ZnO exhibited a strong response to low concentrations of isopropanol, while Co_3O_4–ZnO showed better performance in detecting acetone. Panigrahi *et al.*[7] proposed a nanosensor based on titanium carbide MXenes ($Ti_3C_2T_x$) to detect specific volatile organic compounds (VOCs) present in human breath. A set of representative VOCs,

Department of Chemistry, National Institute of Technology, Calicut Mukkam Road, Kattangal, Calicut, Kerala 673601, India. E-mail: mausumi@nitc.ac.in

including 2,3,4-trimethylhexane, aniline, ethylbenzene, isoprene, and *o*-toluidine, were selected, and their adsorption mechanisms with $Ti_3C_2T_x$ were thoroughly studied using first-principles DFT calculations.

Nanomaterials have emerged as promising candidates for early lung cancer detection due to their high surface-to-volume ratio, enhanced sensitivity, and ability to selectively interact with specific biomarkers.[8] Nanosensors offer non-invasive, rapid, and cost-effective diagnostic tools, contributing to early detection and improved patient outcomes. In 2004, Páez *et al.*[9] conducted both experimental and theoretical studies on the gas sensing capabilities of CNx nanotubes for ethanol, acetone, and ammonia. They found that CNx nanotubes were more effective than pure carbon nanotubes due to the presence of highly reactive pyridine-like sites. Karlický *et al.*[10] investigated the adsorption of various small organic molecules, including acetone, ethanol, dichloromethane, benzene, and toluene, on graphene surfaces using both theoretical and experimental approaches. Aasi *et al.*[11] employed DFT to study the effects of individual toluene molecules on the structural, electronic, and magnetic properties of pristine and metal-decorated Single-Walled Carbon Nanotubes (SWCNTs). Their findings suggested that metal-decorated SWCNT molecular sensors hold promise for the detection of toluene and other lung cancer biomarkers in exhaled breath. Mosahebfard *et al.*[12] studied $MoSe_2$ monolayer as a potential biosensor for early lung cancer diagnosis by examining the adsorption behavior, bandgap modulation, and charge transfer of $MoSe_2$ upon adsorption of biomarkers hexanal, nonanal, and *p*-cresol. Their findings suggest that $MoSe_2$ exhibits promising physisorption properties and reasonable recovery times, making it a potential candidate for further development as a lung cancer biosensor.

In that context, graphitic carbon nitride (g-C_3N_4) is a promising material for gas sensor applications due to its unique properties.[13] It possesses a favorable electronic band structure, high biocompatibility, and easy synthesis. Its large surface area with tunable electronic structures and excellent thermal stability make it suitable for gas sensing.[14] However, the sensing performance of g-C_3N_4 can be further improved through strategies like metal doping, metal oxide/g-C_3N_4 composites, and surface functionalization. g-C_3N_4 exhibits intrinsic defects that act as active sites for gas adsorption. Self-doping with carbon atoms can improve the electrical conductivity of g-C_3N_4 by creating delocalized π-bonds, leading to enhanced electron transfer and reduced bandgap.[15] These combined properties make g-C_3N_4 a promising candidate for gas sensing applications. Bicheng Zhu and co-workers[16] studied CO_2 adsorption on g-C_3N_4 using first-principles calculations. Parthasarathy Srinivasan *et al.*[17] presented a detailed sensing mechanism of g-C_3N_4 as a chemiresistive gas sensor for volatile organic compounds (VOCs), along with the specific rationales for selective detection. They found that optimizing the composition, dopant concentration, loading percentage, and functionalization ratio of g-C_3N_4 with metals and metal oxides can lead to enhanced selectivity, faster response times, and lower detection limits.

Currently, there is increasing research into the sensor capabilities of heterostructures[18–21] and the reasons are manyfold. First of all, the nanoscale effects of heterostructures can significantly influence the band alignment and carrier concentration within the heterostructure, resulting in effective electron–hole separation at the heterojunction. This characteristic is crucial for their potential use in chemical and biological sensors. Secondly, heterostructures allow two different materials to interact with target molecules, enhancing their sensing properties synergistically. By stacking materials with distinct band structures and work functions, it is possible to achieve controlled band alignment at the interface, leading to improved sensing performance and increased selectivity. This enhanced selectivity can be achieved by exploiting the molecular adsorption properties of each component. In view of this, Cao *et al.*[18] created a cocoon-like hybrid nanocomposite of ZnO and graphitic carbon nitride using a simple hydrothermal process and found that the g-C_3N_4/ZnO nanocomposite sensor demonstrated exceptional gas sensing performance for ethanol. It featured a low optimal operating temperature and maintained strong linearity across a broad range of gas concentrations. Wang *et al.*[19] developed a highly efficient acetone sensor using g-C_3N_4/WO_3 nanocomposites and demonstrated its superior performance compared to unmodified WO_3 nanostructures. Zhang *et al.*[20] created g-C_3N_4/SnO_2 composites using a sonication mixing technique, which enhanced the gas sensing properties compared to pure SnO_2. They discovered that the g-C_3N_4/SnO_2 material shows promise as a sensor for acetic acid. Li *et al.*[21] successfully prepared flower-like NiO and g-C_3N_4-decorated NiO composites (Ni/CN) using a straightforward one-step hydrothermal method. They found that the 10 wt% g-C_3N_4(Ni/CN-10) sensor outperformed the pure NiO sensor, showing a nearly threefold increase in response to triethylamine at an optimal temperature of 280 °C. Additionally, the Ni/CN sensor demonstrated improved selectivity and stability, largely due to the incorporation of g-C_3N_4.

Transition metal-based g-C_3N_4 has been reported as a promising material for gas sensing applications. Zhang *et al.*[22] prepared a-Fe_2O_3/g-C_3N_4 nanocomposites using a hydrothermal and pyrolysis method. The formation of heterojunctions in these nanocomposites resulted in improved gas sensing performance compared to pure a-Fe_2O_3 and g-C_3N_4. Gong *et al.*[23] synthesized a ball-flower-like Co_3O_4 composite decorated with carbon nitride using a simple hydrothermal method. The carbon nitride-decorated Co_3O_4 composite demonstrated significantly enhanced ethanol sensing properties, with a response 1.6 times higher than pure Co_3O_4. Additionally, the composite exhibited high selectivity and stability towards ethanol detection. Dong *et al.*[24] developed a Schottky heterojunction sensor modified with g-C_3N_4 quantum dots (g-C_3N_4QDs) and reduced graphene oxide (rGO) deposited on TiO_2 nanotube (TNT) arrays. This sensor demonstrated a high response, exceptionally fast response and recovery times, and outstanding sensitivity for detecting NO_2 at ppb levels at room temperature. Zhang *et al.*[25] successfully synthesized g-C_3N_4-decorated magnesium ferrite ($MgFe_2O_4$) porous microsphere composites using a one-step solvothermal method. The gas-sensing performance of these composites was measured and compared with a sensor based on pure $MgFe_2O_4$. Notably, the

$MgFe_2O_4$/g-C_3N_4 composite sensor with 10 wt% g-C_3N_4 content showed a response to acetone that was enhanced by approximately 145 times, while the optimal operating temperature was reduced by 60 °C. Wang *et al.*[26] developed a one-step hydrothermal method to synthesize a CuO–ZnO/g-C_3N_4 ternary composite. The resulting CuO–ZnO/g-C_3N_4 displayed significantly enhanced ethanol-sensing properties, with responses 1.34 times and 2.17 times higher than those of CuO–ZnO and CuO alone, respectively. This improvement in gas-sensing performance was attributed to the effective p–n junctions between CuO and ZnO, along with the excellent substrate effect of the g-C_3N_4 nanosheets. Sneha *et al.*[27] reported that Co-doping significantly enhanced the gas sensing performance of g-C_3N_4 toward lung cancer biomarkers such as acetone, ethanol, and aniline. Co-g-C_3N_4 exhibited a reduced band gap, improved conductivity, and shorter recovery times—particularly for aniline due to its physisorption nature. These results established Co-g-C_3N_4 as a promising reusable sensor for exhaled breath analysis.

Very recently utilising the DFT calculations, V. N *et al.*[28,29] modelled g-C_3N_4/CoN_4 heterojunction and found that it can act as a type I photocatalyst for water-splitting reactions. Furthermore, in another work, they reported[30] that the same g-C_3N_4/CoN_4 heterojunction while exposed under strain and electric field perturbation switches from type I to type II photocatalyst, which was attributed by the crossover between valence and conduction band in presence of external perturbation. In a more recent work, V. N *et al.*[31] showed that boron and fluorine co-doping of the g-C_3N_4/CoN_4 heterojunction transforms its electronic structure from type-I to a direct Z-scheme, which enhances charge carrier separation and redox ability. This Z-scheme heterojunction is proposed as an efficient photocatalyst for overall water splitting reaction, highlighting the tunability of g-C_3N_4/CoN_4-based systems for energy applications.[32]

In this work, density functional theory (DFT) was employed to systematically investigate the adsorption behavior and electronic response of key aromatic biomarkers—benzene, toluene, aniline, and *o*-toluidine—on both pristine g-C_3N_4 and g-C_3N_4/CoN_4 surfaces. Although g-C_3N_4 had been widely studied as a photocatalyst, its potential for selective gas sensing, particularly when modified with transition metal complexes in the form of a heretojunction is still less explored. Adsorption energetics, electronic structures, charge transfer characteristics, and work function variations were evaluated to gain insights into how functional groups influenced sensor performance. It was revealed that the g-C_3N_4/CoN_4 heterostructure exhibited enhanced sensitivity and selectivity toward aniline, indicating its promise as a potential candidate for real-time detection of breath biomarkers. The *in silico* observation of g-C_3N_4/CoN_4 heterostructure for selective and sensitive detection of aniline vapors is unknown to date.

1.1 Computational methodology

Spin-polarized density functional theory (DFT), as implemented in the Quantum Espresso package, was employed for calculating both the structural optimization and electronic properties[30] of the systems under investigation. The exchange-correlation effects were incorporated using the Perdew–Burke–Ernzerhof (PBE) functional within the Generalized Gradient Approximation (GGA).[33] To address the limitations of GGA functional in handling partially filled d-orbitals and to better account for the localization of d-electrons *via* Coulomb and exchange corrections, the GGA + *U* method was applied, with a U value of 3.4 eV for Co atoms, as supported by several studies.[34] Ultrasoft pseudopotentials were utilized with a plane-wave energy cutoff of 145 Ry, and a vacuum gap of 30 Å was introduced to avoid spurious interactions in the non-periodic *z*-direction. Structural optimization was carried out using the Broyden–Fletcher–Goldfarb–Shanno (BFGS) algorithm, alongside a dispersion-corrected GGA-PBE functional employing the Grimme-D2 scheme.[35] Lattice parameters and atomic positions were optimized until all forces were below 10^{-3} Ry. Phonon spectra of CoN_4 bulk and CoN_4 slab were computed to confirm their lattice-dynamic stability. The unit cell of g-C_3N_4 and CoN_4 were relaxed with k-mesh values of $12 \times 12 \times 1$ and $8 \times 8 \times 8$, respectively.[34] A $2 \times 2 \times 1$ heptazine and $\sqrt{3}\times\sqrt{3} \times 1$ CoN_4 (111) slab with minimal lattice strain and lowest lattice mismatch (δ) were used to model the g-C_3N_4/CoN_4 heterojunction.[30] To understand the chemical sensing of the g-C_3N_4/CoN_4 heterojunction, the gas molecules such as benzene (bz), toluene (bz-CH_3), aniline (bz-NH_2), and *o*-toluidine (NH_2-bz-CH_3) were initially placed approximately at a distance of 3 Å from the surfaces. After completing geometry relaxations, the adsorption energy (E_{ads}), related with each gas adsorption process were calculated using the following formula:[36]

$$E_{ads} = E_{total} - [E_{Heterojunction} - E_{gas\ molecule}] \quad (1)$$

Here, E_{total} is the energy of the g-C_3N_4/CoN_4 heterojunction after adsorption. $E_{gas\ molecule}$ and $E_{Heterojunction}$ are the energy of the individual gas molecules and energy of g-C_3N_4/CoN_4 heterojunction before adsorption, respectively. The charge density difference of the materials under study was examined using GGA-PBE exchange-correlation potential developed in VASP (license number: 22-0418) and DFT-D approach was incorporated for handling van der Waals (vdW) interactions.[37] Bader charge analysis was performed to evaluate the charge transfer (Q_T) between the g-C_3N_4/CoN_4 and each adsorbed biomarker (benzene, toluene, aniline and *o*-toluidine). A negative charge value indicates, transfer of charge from gas molecules to g-C_3N_4/CoN_4 heterojunction. Band structure and projected density of states (PDOS) calculations were done to understand the change in electronic properties after adsorption of biomarkers. To assess the real time application of g-C_3N_4/CoN_4 towards the sensing of biomarkers, work function, sensitivity and recovery time were analysed. Although hybrid functionals such as HSE06 are known to yield more accurate band gaps, their computational cost becomes prohibitive for large heterojunction systems, particularly when considering adsorbed molecules. Therefore, in this work, we employed the GGA + *U* approach, which is widely recognized as a reliable and computationally efficient alternative to mitigate the band-gap underestimation of conventional GGA.

2 Results and discussion

2.1 Structural details of g-C_3N_4, CoN_4, g-C_3N_4/CoN_4 heterojunction and gas molecules

Heptazine-based g-C_3N_4 consists of heptazine (C_6N_7) units arranged in a 2D lattice, where each unit is connected to the others *via* C–N bonds, forming a hexagonal network. The unit cell of this hexagonal lattice comprises 14 atoms, including 8 nitrogen and 6 carbon atoms (Fig. 1(a)). There are two types of carbon atoms, labelled as C1 and C2, each binding with three neighboring nitrogen atoms. The nitrogen atoms are categorized into three types: six N1 atoms with two neighboring carbon atoms, one N2 atom, and one N3 atom, both of which have three neighboring carbon atoms.[38] The optimized lattice parameters for g-C_3N_4 are $a = b = 7.2$ Å, $\alpha = \beta = 90°$, and $\gamma = 120°$, which closely match both XRD experimental values[39] ($a = b = 7.11$ Å) and theoretical predictions[40] ($a = b = 7.2$ Å). The bond lengths for C1–N1, C1–N3, C2–N1, and C2–N2 are 1.33 Å, 1.4 Å and 1.49 Å, respectively, aligning well with previously reported values (1.33, 1.39, and 1.48 Å).[40] The distance between the two nitride pores is 6.91 Å, which is consistent with experimental findings of 6.81 Å.[39] These results validate our computational methods, allowing us to proceed with further investigations.[41]

Next, we considered the diamond-like crystal structure of bulk CoN_4 (Fig. 1(b)), which was optimized using the Generalized Gradient Approximation (GGA) with the Perdew–Burke–Ernzerhof (PBE) functional. The primitive unit cell of CoN_4 was derived from this optimized bulk structure. To confirm the thermodynamic stability of bulk CoN_4, we calculated the formation energy ($E_{formation}$) using the equation:[42]

$$E_{formation}(CoN_4) = \left[\frac{E_{CoN_4}}{2} - \frac{E_{Co}}{2} - 4\frac{E_{N_2}}{8}\right] \Big/ 5 \quad (2)$$

where E_{CoN_4}, E_{Co}, and E_{N_2} are the total energies of CoN_4, Co crystal, and N_2 crystal, respectively. The calculated formation energy of CoN_4 is −0.2064 eV, closely matching the reported value of −0.1992 eV,[42] thus confirming the stability of the CoN_4 system. To check the magnetism associated with CoN_4, the total energies of anti-ferromagnetic (AFM), ferromagnetic (FM) and nonmagnetic (NM) states were calculated to determine the ground magnetic state of CoN_4. The energy values tabulated in Table 1 show that the FM ground state of CoN_4 is more stabilized compared to the AFM state by an amount of 0.5 eV. The stability of the FM state of CoN_4 over the AFM state is agreed with the previous report.[42] We considered the stable FM state for all related calculations.

Table 1 Calculated energies of different magnetic states of CoN_4 bulk

System	Non magnetic state	Ferromagnetic state	Anti-ferromagnetic state
Energy (eV)	0	−2.0	−1.5

The computed lattice parameters for CoN_4 are $a = b = c = 11.4$ Å (Fig. 1(b)), in good agreement with theoretical values ($a = b = c = 11.235$ Å).[45] The bond lengths for Co–N and N–N are 1.89 Å and 1.15 Å, respectively, in line with reported theoretical values (Co–N: 1.84 Å, N–N: 1.18 Å),[42] affirming the reliability of our results.

To construct a realistic heterojunction model combining g-C_3N_4 and CoN_4, we first calculated the surface energy (γ) for the (100), (110), and (111) CoN_4 slabs using the equation:[43]

$$\gamma = \frac{E_{slab} - E_{bulk}}{2A} \quad (3)$$

where E_{slab} and E_{bulk} represent the energies of the CoN_4 slab and bulk, respectively, and A is the slab area. The CoN_4 slabs were created by cleaving the primitive unit cell into (100), (010), and (001) planes, separated by a 30 Å vacuum. The surface energies for the (100), (110), and (111) slabs were found to be 0.36, 0.37, and 0.11 J m^{-2}, respectively, indicating that the (111) slab is the most stable, and was thus selected for the heterojunction formation and subsequent calculations.[43]

The compatibility of the lattice interface (Fig. 1(c)) was ensured by matching a 2 × 2 × 1 heptazine with a $\sqrt{3}\times\sqrt{3}$ × 1 CoN_4 (111) slab. The lattice mismatch (δ) was calculated using the equation:

$$\delta = \frac{a(111) - a(g)}{a(111)} \quad (4)$$

where a(111) and a(g) are the relaxed lattice parameters of the CoN_4 (111) slab and g-C_3N_4 monolayer, respectively. A mismatch of 3% was observed, which was within acceptable limits, consistent with previous reports.[44] The strain in the 2 × 2 × 1 heptazine system was calculated as 0.05%, and in the $\sqrt{3}\times\sqrt{3}$ × 1 CoN_4 (111) slab, it was 2.7%.

After while phonon spectra analysis was performed to check the dynamic stability of CoN_4(111) slab and presented in Fig. 2. Absence of negative frequencies in the phonon spectra in Fig. 2(a) and (b) confirmed the lattice-dynamic stability of CoN_4 bulk and slab. Fig. 2(a) represents the phonon spectra of CoN_4 bulk, which matched with the reported literature and thereby

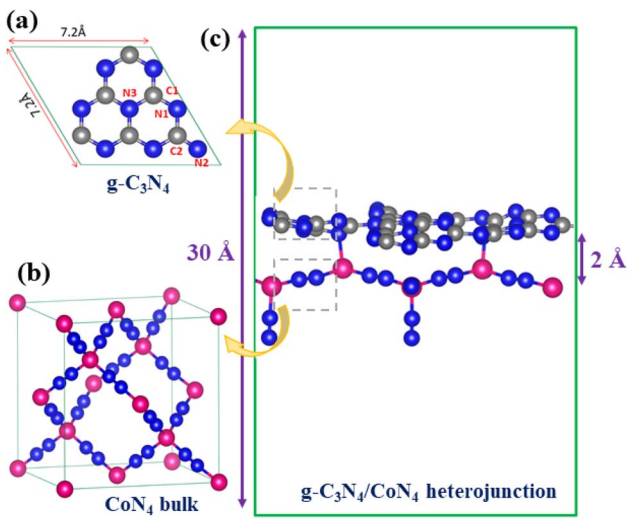

Fig. 1 Optimized geometries of (a) g-C_3N_4 primitive unit cell (b) CoN_4 bulk and (c) g-C_3N_4/CoN_4 heterojunction.

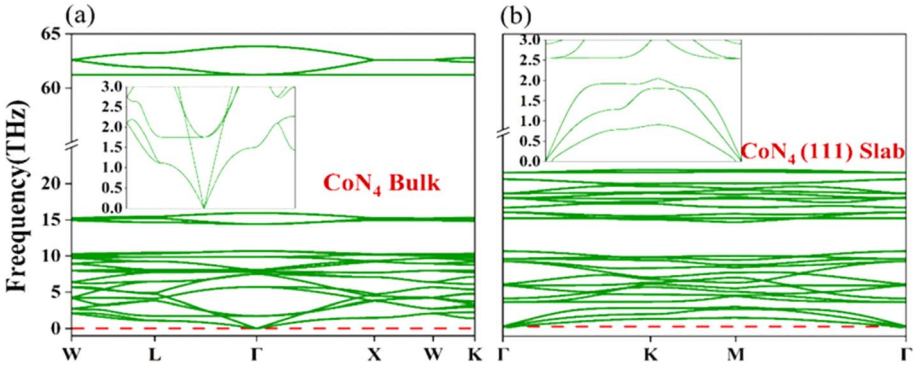

Fig. 2 Phonon spectra of CoN_4 (a) bulk and (b) (111) slab.

confirms the stability of the system as well as reliability of our calculations.[42]

To assess the thermodynamic stability of the heterojunction and the interaction between g-C_3N_4 and CoN_4 (111), the adhesion energy (E_{ad}) was calculated using the equation:[45]

$$E_{ad} = E_{g\text{-}C_3N_4/CoN_4} - E_{g_{C_3N_4}} - E_{CoN_4} \quad (5)$$

where $E_{gC_3N_4/CoN_4}$, $E_{gC_3N_4}$, and E_{CoN_4} represent the total energies of the relaxed g-C_3N_4/CoN_4 heterostructure, g-C_3N_4 monolayer, and CoN_4 (111) slab, respectively. The calculated negative adhesion energy of −4.7396 eV indicates that the adsorption process is thermodynamically stable, making the adhesion of CoN_4 onto the g-C_3N_4 surface exothermic and energetically favorable.[28]

The C–C bond length in benzene (Fig. S1(a)), the C1–C2 and C2–C3 bond length in toluene (Fig. S1(b)), the C–N bond length in aniline (Fig. S1(c)) and the C5–C6 bond length in *o*-toluidine (Fig. S1(d)) were measured as 1.399 Å, 1.403 Å,1.398 Å, 1.395 Å, and 1.396 Å respectively. The C–C–C bond angle in benzene, C6–C1–C2 in toluene, N–C–C in aniline, and N–C1–C6 in *o*-toluidine were found to be, 119°54′,119.40°, 120.00° and 118.9° respectively. These calculated bond length and bond angle of aniline align with the earlier study by Vaschetto *et al.*[46] where reported C–N bond length and N–C–C bond angle were of 1.392 Å and 120°. Similarly, the geometrical parameters of benzene are in good agreement with earlier study by Koichi Tamagawa *et al.*[47] and E. G. Cox,[48] where they reported a C–C bond length of 1.399 Å and C–C–C bond angle of 119°28′. The bond length and bond angle values for toluene are consistent with the study by David R Borst *et al.*,[49] they noted a C1–C2 bond length of 1.397 Å, C2–C3 bond length of 1.394 Å and C6–C1–C2 bond angle of 119.40°. The parameters of *o*-toluidine are aligned with the study by V. K. Bel'skii *et al.*[50] which reported a C6–C5 bond length of 1.389 Å and a N–C1–C6 bond angle of 120.3°. The bond lengths and bond parameters are presented Table S1.

2.2 The adsorption of selected gas molecules on the g-C_3N_4

Before exploring the adsorption of gas molecules on the g-C_3N_4/CoN_4 heterojunction, we first calculated the adsorption energies of gas molecules on pristine g-C_3N_4. The adsorption of biomarkers such as benzene, toluene, aniline, and *o*-toluidine was examined and the resulting adsorption energies are presented in Table 2. The most stable configurations for g-C_3N_4/benzene, g-C_3N_4/aniline, g-C_3N_4/*o*-toluene, and g-C_3N_4/*o*-toluidine are shown in Fig. 3. The adsorption energies for g-C_3N_4 interacting with various aromatic molecules – benzene, toluene, aniline, and *o*-toluidine – are −1.51 eV, −1.87 eV, −0.98 eV, and −2.03 eV, respectively. Notably, the adsorption energy of g-C_3N_4 with *o*-toluidine is the highest among these, indicating a stronger interaction. Aniline is physisorbed on the g-C_3N_4 surface, whereas the other gas molecules are chemisorbed on the g-C_3N_4 surface. The intermolecular distances between the gas molecules and g-C_3N_4 are illustrated in the Fig. 3 The distance between g-C_3N_4 and benzene is 3.10 Å. Due to the presence of a methyl group, the distance between toluene and g-C_3N_4 decreases to 2.67 Å compared to benzene. However, the nitrogen in aniline causes a slight repulsion with g-C_3N_4, increasing the distance to 3.12 Å. In contrast, the additional methyl group in *o*-toluidine results in a shorter distance from g-C_3N_4 (2.95 Å) compared to aniline.

After calculating the adsorption energy, the sensing potential of pristine g-C_3N_4 was evaluated, by calculating the recovery times of four biomarkers on the g-C_3N_4 surface using the following equation:[46]

$$\tau = \nu_o^{-1} \exp\left[-E_{ads}/k_B T\right] \quad (6)$$

where ν_o represents the attempt frequency (a constant of 10^{12}) for visible light, T is the temperature, and k_B is the Boltzmann constant. The calculated recovery times for benzene, toluene, aniline, and *o*-toluidine gas molecules on the pristine g-C_3N_4 surface are 3.52×10^{13} s, 4.33×10^{19} s, 3.80×10^{4} s, and $2.58 \times$

Table 2 Adsorption energy of benzene, toluene, aniline and *o*-toluidine biomarkers adsorbed on g-C_3N_4 unit

System	g-C_3N_4/benzene	g-C_3N_4/toluene	g-C_3N_4/aniline	g-C_3N_4/*o*-toluidine
Adsorption Energy (eV)	−1.51	−1.87	−0.98	−2.03

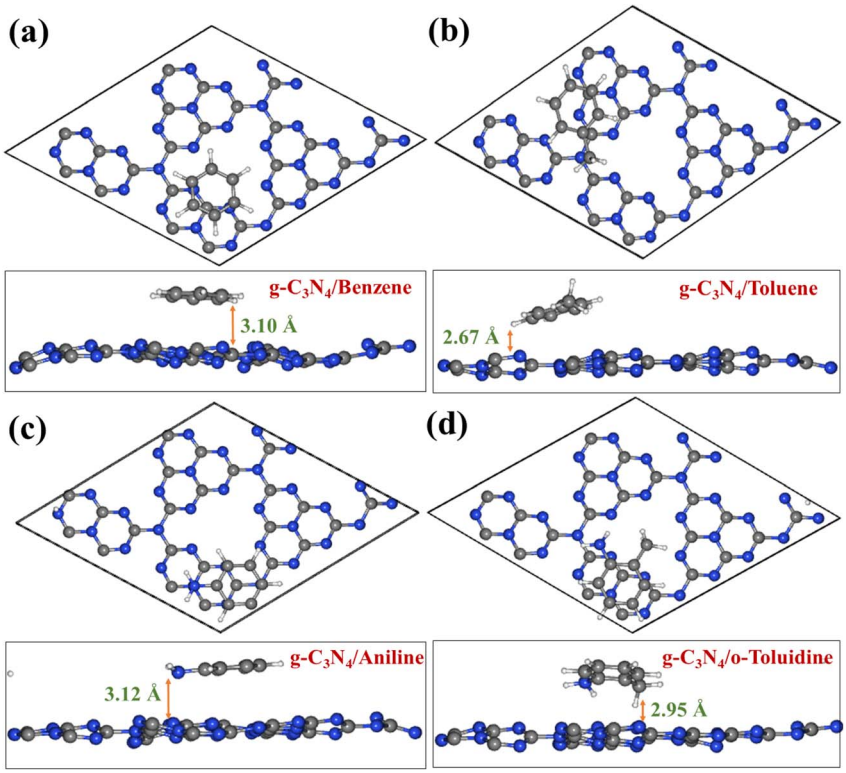

Fig. 3 Optimised structures of biomarkers (a) benzene, (b) toluene (c) aniline and (d) *o*-toluidine adsorbed on the g-C_3N_4 surface.

10^{22} s, respectively. A close examination of these values reveals that the recovery times are excessively long, making it impractical to desorb these gas molecules at room temperature.

In that context, research has shown that incorporating metal atoms can significantly enhance the sensing capabilities of materials.[47,48] Therefore, to improve the sensing ability of g-C_3N_4, it was combined with CoN_4, and a detailed investigation of the adsorption behavior and sensor activity of the g-C_3N_4/CoN_4 heterojunction was conducted.

2.3 Optical band gap of g-C_3N_4 and g-C_3N_4/CoN_4

The optical band gap of g-C_3N_4 was calculated using Tauc's method,[49] as described by the equation:

$$(\alpha h\nu)^{m} = A_0\left(h\nu - E_g^{opt}\right) \quad (7)$$

where α is the absorption coefficient, $h\nu$ is the energy of the incident photon, E_g^{opt} represents the optical band gap, and A_0 is a constant that is related to the transition probability. The optical band gap is presented in Fig. 4. From Fig. 4, the calculated optical band gap of g-C_3N_4 is determined to be 2.58 eV, which is in close agreement with the experimentally reported value of 2.65 eV.[50] Similarly, the optical band gap of g-C_3N_4/CoN_4 was found as 2.06 eV (see Fig. 4). The optical band gaps of g-C_3N_4 and g-C_3N_4/CoN_4 have been plotted in Fig. 4. The optical absorption maxima of g-C_3N_4 and g-C_3N_4/CoN_4 are 480 nm and 602 nm,[28,29] respectively (see the vertical line in Fig. 4). The red shift in the optical absorption maximum of the g-C_3N_4/CoN_4 heterojunction compared to g-C_3N_4 indicates enhanced light absorption and more effective sensing ability compared to pristine g-C_3N_4. The red-shifted absorption maximum of the heterojunction and higher recovery time of the gas molecules on pristine g-C_3N_4, motivated to investigate the sensor activity of the g-C_3N_4/CoN_4 heterojunction.

2.4 The adsorption of selected gas molecules on the g-C_3N_4/CoN_4

To simulate the adsorption process, we positioned each gas molecule under investigation such as benzene, toluene, aniline, and *o*-toluidine on various potential sites of g-C_3N_4/CoN_4

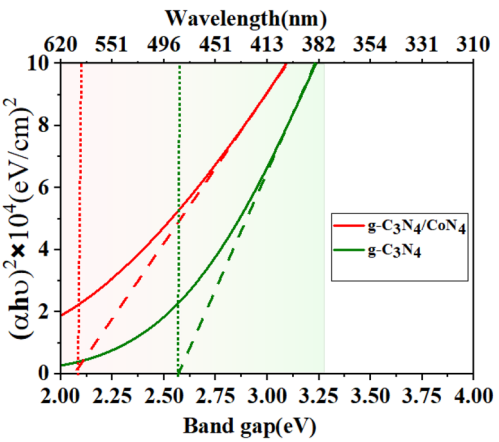

Fig. 4 Optical band gap of pristine g-C_3N_4 and g-C_3N_4/CoN_4.

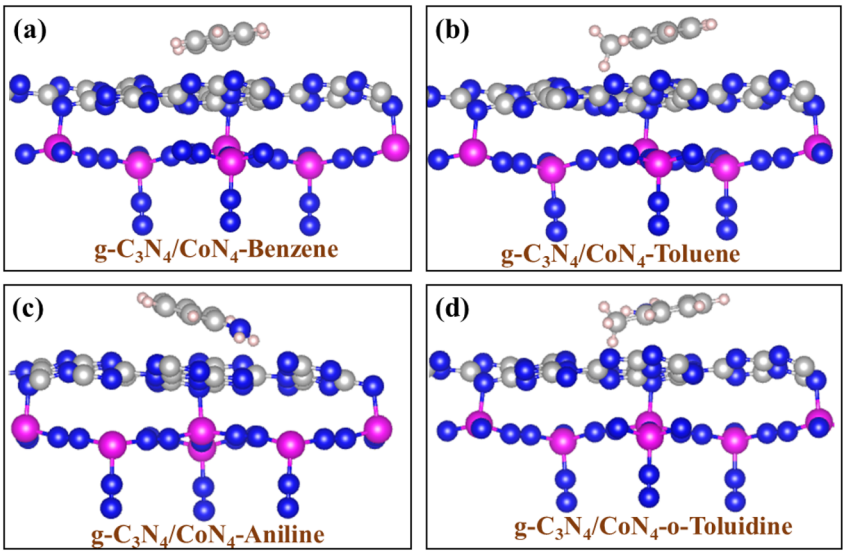

Fig. 5 Optimised structures of biomarkers (a) benzene, (b) toluene (c) aniline and (d) *o*-toluidine adsorbed on the g-C_3N_4/CoN_4 heterojunction.

heterosurface. At the very first point the most favorable adsorption points for each gas molecule on the 2D system was determined. The g-C_3N_4/CoN_4 + gas molecules in their ground states were optimized considering all probable possibilities, and the most stable configurations was identified based on the adsorption energies calculated using eqn (1). These stable structures of g-C_3N_4/CoN_4 heterojunction with gas molecules are presented in Fig. 5 and the adsorption energies are summarized in Table 3. The adsorption sites on the g-C_3N_4/CoN_4 heterojunction was found to be varied depending on the gas molecules involved, with each molecule occupying a distinct site. Notably, all gas molecules prefer to adsorb absolutely on the g-C_3N_4 layer of the heterojunction. For benzene, the adsorption energy was −0.67 eV, and it preferred mostly to align on void of the g-C_3N_4. Toluene adsorbs with an energy of −0.84 eV, positioning its CH_3 group projecting into the g-C_3N_4 void. Aniline binds the heterojunction with an adsorption energy of −0.97 eV, with its NH_2 group oriented into the void. Similarly, *o*-toluidine adsorbs with an energy of −1.08 eV, positioning both its CH_3 and NH_2 groups within the g-C_3N_4 void. Notably, the adsorption energy in case of physisorption, generally ranges from −0.5 eV to −1.0 eV. Based on these values, benzene, toluene, and aniline display physisorption behavior on the g-C_3N_4/CoN_4 heterojunction, while *o*-toluidine lies on the borderline between physisorption and chemisorption. This major advantage of physisorption is that – it enables the g-C_3N_4/CoN_4 heterojunction to function as a reusable sensor. Interestingly, while the ring electron density of the gas molecules follows the order benzene < toluene < aniline < *o*-toluidine.

The adsorption energies tabulated in Table 3 clearly reveals that benzene showed weak adsorption while *o*-toluidine adsorbed strongly on the g-C_3N_4/CoN_4 surface. Consequently, the adsorption energy of the gas molecules followed an order as benzene < toluene < aniline < *o*-toluidine. This can be attributed by the electron density of the gas molecules: benzene, being the least electron-rich, has a lower tendency to donate electrons to the g-C_3N_4/CoN_4 heterojunction, resulting in a lower adsorption energy. In contrast, *o*-toluidine is having the highest electron-density due to the presence of two electron-donating groups (CH_3 and NH_2), which enhanced its electron-donating capability and lead to a higher adsorption energy towards heterojunction surface. Toluene and aniline are positioned in between the two terminals as their electron density are higher compared to benzene but lowered compared to *o*-toluidine. These calculated adsorption energies vis-à-vis the direction and magnitude of charge transfer has been discussed in the next section.

The prime criteria of a gas sensor to achieve optimal sensing performance is that the interactions between the adsorbent and the gas molecules must be sufficiently strong to generate measurable signals for detection. However, the gas molecules should also be able to desorb from the sensor without altering its properties, allowing for quick recovery. It is important to highlight that the adsorption energy of gas molecules is relatively high, ensuring stability against thermal fluctuations at room temperature ($k_BT = 0.025$ eV).[49]

The calculated adsorption energy for benzene is −0.67 eV, which lies within the optimal range of −0.60 to −1.0 eV for reversible gas capture. Although this value is less negative than

Table 3 Adsorption energy of benzene on g-C_3N_4/CoN_4, toluene on g-C_3N_4/CoN_4, aniline on g-C_3N_4/CoN_4 and *o*-toluidine on g-C_3N_4/CoN_4

System	g-C_3N_4/CoN_4-benzene	g-C_3N_4/CoN_4-toluene	g-C_3N_4/CoN_4-aniline	g-C_3N_4/CoN_4-*o*-toluidine
Adsorption Energy (eV)	−0.67	−0.84	−0.97	−1.08

the literature value reported by Yaseen *et al.*[52] (−0.93 eV) for benzene adsorbed on a Pt-cluster modified g-C_3N_4 nanosheet, the observed trend remains consistent, indicating moderate interaction strength suitable for sensor applications. For toluene, our computed adsorption energy is −0.84 eV, falling within the optimal window. However, Aasi, A. *et al.*[53] reported a significantly stronger adsorption energy of −1.3 eV for toluene on a Pd-decorated carbon nanotube (CNT) surface. In the case of aniline, our result of −0.97 eV compares reasonably with those reported by Panigrahi, P. *et al.*,[54] who studied aniline adsorption on various Ti_3C_2 MXene-based surfaces: $Ti_3C_2F_2$ (−0.663 eV), $Ti_3C_2(OH)_2$ (−1.052 eV) and $Ti_3C_2O_2$ (−1.031 eV).

For *o*-toluidine, the calculated adsorption energy of −1.08 eV lies just outside the ideal window, indicating relatively strong adsorption. Panigrahi, P. *et al.*[54] report a range of values on the same Ti_3C_2-based surfaces: $Ti_3C_2F_2$ (−0.691 eV), $Ti_3C_2(OH)_2$ (−0.942 eV) and $Ti_3C_2O_2$ (−1.158 eV) Overall, the adsorption energies of benzene, toluene, aniline and *o*-toluidine biomarkers on the g-C_3N_4/CoN_4 heterojunction demonstrate strong agreement with literature values, confirming their relevance for reversible gas capture applications.

2.5 Charge density difference

It is commonly understood that the sensing mechanism in 2D materials is primarily driven by charge transfer, which plays a key role in altering the resistance across sensing channels during gas adsorption. To analyze the distribution of electrons at the gas-surface interface, we employ charge density difference (CDD) calculations using the given formula.[55]

$$(\Delta\rho = \rho_{gC_3N_4/CoN_4\_gas} - \rho_{gC_3N_4/CoN_4} - \rho_{gas}) \quad (8)$$

Here $\Delta\rho$ is the charge density difference. $\rho_{gC_3N_4/CoN_4\_gas}$, $\rho_{gC_3N_4/CoN4}$and ρ_{gas} are the electronic charge of gC_3N_4/CoN_4_gas, gC_3N_4/CoN_4 and gas molecules (of benzene, toluene, aniline and *o*-toluidine) respectively.

Fig. 6 represents 3D charge density difference plots ($\Delta\rho$) along the *z*-axis. The iso-surface value for all targeted gas molecules was set to 0.0002e Å^{-3} in the 3D plots to maintain the consistency which ensures the graphs are on the same scale. This allows us to easily observe the regions of charge accumulation and depletion, and provide valuable insights into the charge transfer process. Generally, a higher or lower iso-surface value indicates areas with greater or lower electron density, respectively. The figure illustrates distinct electron-rich (yellow) and electron-deficient (cyan) regions. Notably, in all cases, the gas molecules exhibit a predominance of electron-deficient areas, while the heterojunctions show a dominance of electron-rich areas. This suggests a potential electron transfer mechanism from the gas molecules to the heterojunction. The electron density of the gas molecules is directly proportional to the charge transfer, which is clearly visible in the charge density difference plot. In all cases, both electron-rich and electron-deficient regions are present in both the gas molecules and the heterojunctions. Fig. 6 consequently, indicates that the high electron density of *o*-toluidine leads to a significant charge transfer within the system. To quantify the extent of electron transfer, we performed Bader charge analysis. The calculated charge transfers for benzene, toluene, aniline, and *o*-toluidine were found to be 0.0260|*e*|, 0.0237|*e*|, 0.0238|*e*|, and 0.0610|*e*| respectively. Notably, a clear direct relationship exists between the amount of charge transfer and the electron density of the gas molecules. Benzene, being the highest electron deficient, exhibits the lowest charge transfer compared to the other molecules. This reduced electron donation propensity is attributed to the lower electron density of benzene, which hinders electron transfer to the heterojunction. Due to the presence of two electron donating groups *o*-toluidine shows an exceptionally high amount of charge transfer. The highest electron transfer of *o*-Toluidine may be due to the higher adsorption energy of *o*-Toluidine on the heterojunction.

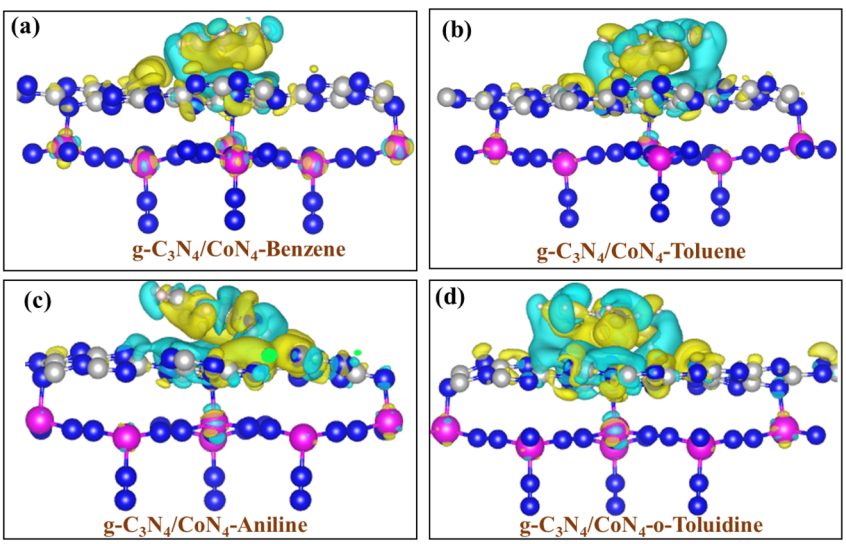

Fig. 6 Charge density difference plots of biomarkers (a) methanol, (b) ethanol (c) acetone and (d) aniline adsorbed on the g-C_3N_4/CoN_4 heterojunction.

2.6 Band structure

To understand the influence of gas molecule adsorption on the electronic properties of the g-C_3N_4/CoN_4 heterojunction, we have calculated the electronic properties, including the band structure, total density of states (TDOS), and partial density of states (PDOS) of both the heterojunction and the heterojunction with adsorbed molecules.

Fig. 7 presents the band structure of g-C_3N_4/CoN_4 heterojunction and the same with adsorbed gas molecules. As already reported g-C_3N_4/CoN_4 is half metallic in nature[27,28] where spin up channel (purple in Fig. S2 in SI file) behaves as semiconductor and spin down channel acting as a metal. The g-C_3N_4/CoN_4 heterojunction exhibits a direct bandgap of approximately 1.81 eV, from the Γ point of conduction band minimum (CBM) to the Γ point valence band maximum (VBM)

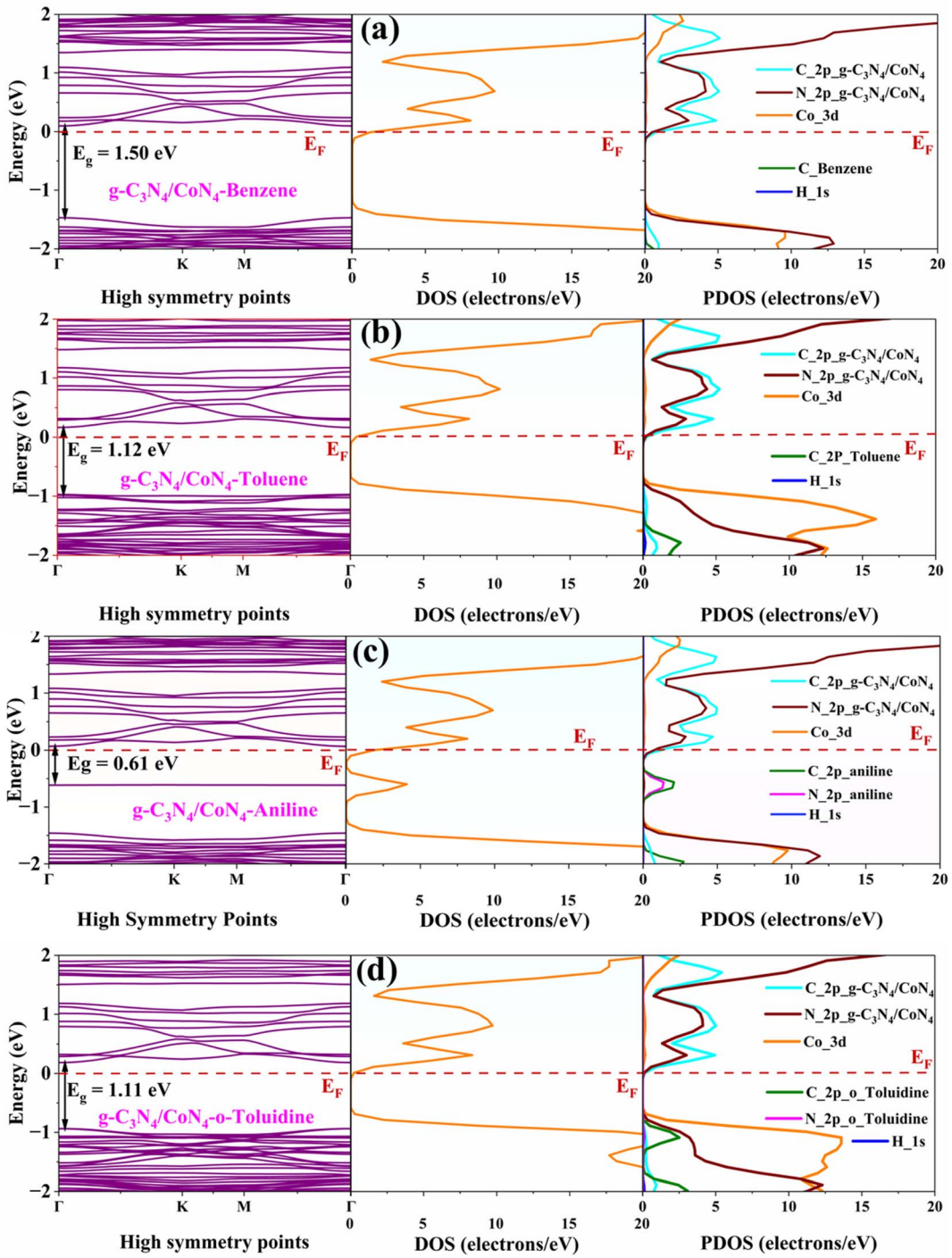

Fig. 7 Band structure (spin up), DOS (spin up) and PDOS (spin up) of biomarkers (a) benzene, (b) toluene (c) aniline and (d) *o*-toluidine adsorbed on the g-C_3N_4/CoN_4 heterojunction.

(see Fig. 7), which aligns with previously reported values.[30] This bandgap energy of g-C_3N_4/CoN_4 heterojunction falls within the visible light spectrum, indicating that visible light exposure could enhance the VOC sensing efficiency, similar to organic molecules and ZnO gas sensors functionalized with organic compounds.[56,57]

To further understand the gas adsorption behavior on g-C_3N_4/CoN_4, electronic band structures were obtained for the gas-adsorbed systems, as illustrated in Fig. 7. Band structures of all the gas-adsorbed systems are half metallic in nature. Gas adsorption was found to influence the electronic properties of the g-C_3N_4/CoN_4 heterojunction. The pristine g-C_3N_4/CoN_4 has an energy gap of about 1.81 eV, which changes upon gas adsorption. The band gap values after the adsorption of benzene, toluene, aniline, and *o*-toluidine were 1.50, 1.12, 0.61 and 1.11 eV, respectively, indicating variations of 0.31, 0.69, 1.20 and 0.70 eV for each gas. This suggests that the adsorption of benzene has minimal impact on the band structure near the Fermi level. However, the adsorption of aniline has the greatest impact on the band structure near the Fermi level. Despite these changes, the direct bandgap nature of g-C_3N_4/CoN_4 remains intact. The change in the band gap due to benzene adsorption is notably lower compared to other gas molecules. This is because benzene has a lower electron density than the other gases, resulting in a reduced tendency to adsorb on the surface of g-C_3N_4/CoN_4 heterojunction. Consequently, benzene's weak adsorption impacts the heterojunction's band gap minimal.

The calculated band gap change of 0.31 eV for benzene indicates a strong interaction between the adsorbate and the material surface, suggesting its suitability for gas sensing applications. This shift is significantly higher than the 0.21 eV reported by Jyothi *et al.*[58] for benzene on 4–8 hBN NT, and the 0.005 eV reported by Phung *et al.*[59] for benzene on graphene, implying enhanced sensitivity in the present system. For toluene, a notable band gap change of 0.69 eV is observed, indicating a strong interaction with the heterostructure. This value substantially exceeds the literature-reported shifts of 0.016 eV and 0.024 eV by Aasi *et al.*,[53] corresponding to toluene adsorption on Pt-SWCNT and Pd-SWCNT, respectively, thereby demonstrating superior sensing potential. In the case of aniline, the observed band gap modulation of 1.2 eV reflects an exceptionally strong electronic interaction, which could result in significant changes in electrical properties even at low analyte concentrations. This is considerably larger than the 0.11 eV reported by Zhang *et al.*[60] for aniline on Pd–ZnO, highlighting improved sensing characteristics. For *o*-toluidine, the computed band gap change of 0.7 eV further supports the material's enhanced sensing ability. This is significantly higher than the 0.185 eV reported by Wan *et al.*[61] for *o*-toluidine adsorption on Ir-doped CNTs, reinforcing the improved response in the current study. Due to the highest observed band gap change, the g-C_3N_4/CON_4 heterostructure exhibits superior sensitivity towards aniline, making it a highly promising candidate for selective aniline gas sensing compared to other analyte molecules. Overall, the larger band gap shifts observed in this work compared to literature values underscore the stronger adsorbate-material interactions and suggest that the studied heterostructure is a promising platform for high-performance gas sensor applications.

To gain a clear understanding of the electronic properties of the systems under investigation, the total density of states (TDOS) and partial density of states (PDOS) of the systems were calculated and presented in Fig. 7. The band gap reduction of the heterojunction in the presence of gas molecules is clearly visible in the TDOS plots. By analyzing the PDOS of the g-C_3N_4/CoN_4 heterojunction, it can be concluded that the valence band maximum (VBM) of the heterojunction is primarily composed of C 2p and N 2p orbitals, while the conduction band minimum (CBM) is dominated by Co 3d and N 2p orbitals.[28,29] In the cases of g-C_3N_4/CoN_4-benzene, g-C_3N_4/CoN_4-toluene, and g-C_3N_4/CoN_4-*o*-toluidine, the valence band maximum (VBM) and conduction band minimum (CBM) remain consistent with those of the g-C_3N_4/CoN_4 heterojunction. However, for g-C_3N_4/CoN_4-aniline, while the VBM aligns with that of the g-C_3N_4/CoN_4 heterojunction, the CBM is primarily composed of N 2p and C 2p orbitals from the aniline molecule. Due to the presence of aniline orbitals interposed between those of the heterojunction, the band gap of g-C_3N_4/CoN_4-aniline is significantly reduced compared to the other systems. When gas molecules adsorb onto the g-C_3N_4/CoN_4 heterojunction, their orbitals hybridize with those of the heterojunction, facilitating strong interactions. For example, when benzene is adsorbed, the C 2p orbitals of benzene overlap with the C 2p orbitals of the heterojunction at the valence band maximum (VBM), while the H 1s orbitals of benzene interact with the Co 3d orbitals at the conduction band minimum (CBM). Similarly, in the case of toluene, both the C 2p and H 1s orbitals of toluene hybridize with the C 2p orbitals of the heterojunction at the VBM, and the H 1s orbitals of toluene overlap with the Co 3d orbitals at the CBM. Additionally, when *o*-toluidine adsorbs onto the heterojunction, the C 2p orbitals of *o*-toluidine hybridize with those of the heterojunction at the VBM, while the N 2p orbitals of *o*-toluidine interact with the C 2p orbitals of the heterojunction at the CBM. There is significant overlap between the PDOS peaks of aniline (especially C-2p and N-2p of aniline) and the g-C_3N_4/CON_4 substrate (C-2p, N-2p, Co-3d), indicating strong electronic coupling and orbital hybridization. This pronounced interaction suggests that the g-C_3N_4/CON_4 heterostructure is particularly well-suited for selective aniline detection, outperforming its sensing performance for other gas molecules. These orbital interactions significantly enhance the adsorption properties and electronic characteristics of the g-C_3N_4/CoN_4 heterojunction, making it a promising material for applications in gas sensing and catalysis.

2.7 Gas sensing device evaluation

2.7.1 Sensitivity. The development of an effective gas-sensing device requires meeting several key criteria, such as high sensitivity, reliable selectivity, and fast response and recovery times. For this reason, a gas sensor based on the g-C_3N_4/CoN_4 heterojunction must exhibit strong adsorption energies for potential target gases. Additionally, the sensor should demonstrate ideal charge transfer to influence electrical

conductivity. Our calculations suggest that the g-C_3N_4/CoN_4 heterostructure has sufficient adsorption energy for benzene, toluene, aniline and *o*-toluidine, preventing spontaneous desorption at room temperature. Electronic calculations revealed that all adsorbate-covered surfaces showed significantly lower band gap energies compared to the pristine heterostructure. This finding suggests that adsorption has a pronounced impact on the electronic properties of the heterostructure. As a result, gas molecules can be identified by analyzing the changes in electrical conductivity observed before and after the adsorption process. Sensitivity, a crucial aspect of gas sensing, can be addressed by evaluating changes in electrical conductivity using the equation,[62]

$$\sigma \sim \exp[-E_g/2k_BT] \quad (9)$$

where σ, E_g, T and k_B are the electrical conductivity, band gap, temperature, and Boltzmann constant (8.62×10^5 eV K^{-1}), respectively. At room temperature of 298 K, the pristine g-C_3N_4/CoN_4 heterojunction has an electrical conductivity of 6.3×10^{-16}. After adsorption, the conductivity values for benzene, toluene, aniline and *o*-toluidine gases were determined and shown in Table 4. The electrical conductivities of benzene, toluene, aniline and o-toluidine are 2.08×10^{-13}, 3.40×10^{-10}, 6.94×10^{-6} and 4.13×10^{-10} respectively. Based on these calculations, we found that the conductivity of the adsorbate systems was higher than that of the pristine g-C_3N_4/CoN_4 heterostructure, with the most significant change in conductivity occurring in the case of aniline (6.94×10^{-6}). Combined with the higher band gap change and strong orbital hybridization observed in the PDOS analysis, this suggests that the g-C_3N_4/CON_4 heterojunction can act as an excellent sensor for aniline detection. This reduction in conductivity may be attributed to benzene's lower electron ring density, which weakens its interaction with the heterojunction and thereby limits charge transfer ($0.0260|e$), leading to lower conductivity.

2.7.2 Recovery time. To know the reusability of the sensor the recovery time was calculated in the next step. Recovery time is the minimum time required for a sensor to desorb the adsorbed gas from its surface. Higher adsorption energy leads to difficulty in desorption process thereby prolonging the recovery time. It can be obtained from the transition state theory and van't Hoff Arrhenius equation which is given in eqn (8).

The recovery time for each species at room temperature (T = 298 K), has been presented in Table 4. The foremost criterion of reversible gas capture is that – optimal adsorption energies should be typically fall within the range of −0.60 to −1.0 eV. A higher adsorption energy (E_{ads}) makes gas desorption more challenging, though an increase in temperature would greatly speed up the process. The recovery time, ranging from milliseconds to a few seconds, indicates the reusability of the gas sensor. However, if the recovery time is too short, it may imply insufficient adsorption capability, which hinders effective gas detection. The adsorption energies of benzene, toluene, aniline, and *o*-toluidine on the heterojunction range from −0.60 to −1.0 eV. The recovery times for benzene, toluene, aniline and *o*-toluidine were calculated as 0.216 s, 162.71 s, 3.18×10^3 s, and 1.86×10^6 s, respectively. Therefore, the heterojunction undoubtedly functions as an efficient reusable sensor for the detection of benzene, toluene, aniline and *o*-toluidine. The recovery time of the g-C_3N_4/CoN_4 heterojunction is significantly shortened when benzene is adsorbed onto it. This faster recovery may be attributed to benzene's lower ring electron density, which weakens its interaction with the heterojunction, thereby reducing charge transfer and facilitating a quicker desorption process. Consequently, the limited interaction results in a lower impact on conductivity, allowing the system to return to its baseline state more efficiently.

The computed recovery time of 0.216 s for benzene adsorption on the g-C_3N_4/CON_4 heterostructure is remarkably shorter than the 5.32×10^3 s reported by Yaseen *et al.*[52] for benzene on Pt-g-C_3N_4, showcasing a significant advancement in gas sensing performance with rapid sensor reset capabilities. For toluene, the calculated recovery time of 162.71 s is substantially lower than the 5.85×10^6 s reported by Nagarajan *et al.*[63] for toluene detection using ring-silicon-doped twisted bilayer arsenene nanosheets (ASNS), revealing a drastic enhancement in sensing efficiency. The improved desorption behavior underlines the heterostructure's potential for high-throughput gas sensing applications. Rahman *et al.*[64] reported that the recovery time of aniline on AINNT (aluminium nitride nanotube) is in the order of 10^{35}, while that on AIPNT (aluminium phosphide nanotube) is in the order of 10^{23}. In contrast, our calculated recovery time for aniline on the g-C_3N_4/CoN_4 system is on the order of 10^3, which is significantly lower than the values reported by Rahman *et al.*[64] This clearly indicates that our material can act as an efficient sensor for aniline. Overall, the considerable reduction in recovery times compared to previously reported materials confirms that the g-C_3N_4/CON_4 heterojunction offers exceptional performance, making it a promising candidate for

Table 4 Recovery time and conductivity of benzene, toluene, aniline and *o*-toluidine while adsorbed on g-C_3N_4/CoN_4

Biomarkers	Recovery time (s) at 298K	Conductivity
Benzene	0.216	2.08×10^{-13}
Toluene	162.71	3.40×10^{-10}
Aniline	3.18×10^3	6.94×10^{-6}
o- oluidine	1.86×10^6	4.13×10^{-10}

Table 5 Work functions of benzene, toluene, aniline and *o*-toluidine on g-C_3N_4/CoN_4

Gas molecule	Work function(Φ)	Change in work function (ΔΦ)
g-C_3N_4/CoN_4	4.56	
Benzene	4.24	−0.32
Toluene	4.59	+0.03
Aniline	4.34	−0.22
o-Toluidine	4.62	+0.06

sensitive, fast, and reusable gas sensors suited for real-world applications.

2.7.3 Work function. To know the effect of adsorption on the work function of the heterojunction we have calculated the work functions of the heterojunction and adsorbed systems. The work function (Φ) represents the minimum energy needed to remove an electron from the surface of material to vacuum and given by:[51]

$$\varnothing = E_{vac} - E_F \quad (10)$$

Here, E_{vac} is the vacuum level energy and E_F is the Fermi level energy. The work function, therefore, being a surface property could also be used to understand the sensing capability of sensor materials. The variations in work function upon adsorption was studied by Gilani and coworkers, which shows that DFT calculations can reasonably predict the changes in work function induced by physisorbed gases.[55] The adsorbed gas molecules in the present study may alter the work function of the g-C_3N_4/CoN_4. In order to get deeper insight about the sensing capacity, the work function of g-C_3N_4/CoN_4 after adsorption of benzene, toluene, aniline and *o*-toluidine gas molecules was calculated. The work function of isolated g-C_3N_4/CoN_4 as well as the same after adsorption of gas molecules is given in Table 5. Our calculations predict that the work function of the isolated g-C_3N_4/CoN_4 heterostructure is 4.56 eV, slightly higher than that of graphene (4.5 eV). As shown in Table 5, the adsorption of toluene and *o*-toluidine increases the work function by 0.03 eV and 0.06 eV respectively, indicating that electron transfer to the vacuum level is hindered by adsorption. In contrast, the adsorption of other molecules, such as benzene (by 0.32 eV) and aniline (by 0.22 eV), reduces the work function. Thus, the work function of the heterostructure can be effectively modified by the presence of these gas molecules.

3 Conclusion

In this study, we employed density functional theory (DFT) calculations to investigate the adsorption behavior of lung cancer–related volatile organic compounds (VOCs)—benzene, toluene, aniline, and *o*-toluidine—on pristine g-C_3N_4 and its CoN_4-modified composite (g-C_3N_4/CoN_4 heterojunction). Our results reveal that CoN_4 incorporation substantially enhances the chemical reactivity of g-C_3N_4, leading to stronger interactions and improved electronic responses toward the target molecules. While benzene, toluene, and aniline exhibit reversible adsorption on g-C_3N_4/CoN_4 heterojunction, enabling potential sensor reusability, *o*-toluidine binds irreversibly. Among the studied VOCs, aniline demonstrated the most pronounced electronic and conductivity changes, establishing g-C_3N_4/CoN_4 as a highly selective and sensitive candidate for aniline detection.

The key take-home message of this work is that rational surface engineering of g-C_3N_4 with transition-metal sites such as CoN_4 can transform an otherwise moderate adsorbent (such as g-C_3N_4) into a highly promising material (by forming g-C_3N_4/CoN_4 heterojunction) platform for breath-based biomarker sensing. These insights not only highlight aniline as a reliable target VOC for theoretical screening but also provide predictive guidelines for experimental validation and device development. Future efforts should focus on integrating g-C_3N_4/CoN_4 composites into real sensor architectures and benchmarking their performance under realistic conditions, thereby advancing non-invasive diagnostic tools for lung cancer.

Conflicts of interest

There are no conflict of interest to declare.

Data availability

All data used in the research article can be obtained from the corresponding author upon reasonable request. Data for this article are available at https://zenodo.org/records/17707981.

Supplementary information (SI): optimised structures of biomarkers, bond parameters of gas molecules and the band structure of g-C_3N_4/CoN_4 heterojunction. See DOI: https://doi.org/10.1039/d5ra04202j.

Acknowledgements

M. Chattopadhyaya acknowledges the SERB POWER GRANT (Fileno. SPG/2021/004752) for providing the funding of the project. Dhilshada. V. N acknowledges the UGC for providing the fellowship grant. Shilpa M acknowledges NIT Calicut for financial support. The author M. Chattopadhyaya also acknowledges the center for Computational Modelling and Simulation (CCMS), NIT Calicut, for computational support.

References

1 W. Li, H.-Y. Liu, Z.-R. Jia, P.-P. Qiao, X.-T. Pi, J. Chen and L.-H. Deng, Advances in the Early Detection of Lung Cancer Using Analysis of Volatile Organic Compounds: From Imaging to Sensors, *Asian Pac. J. Cancer Prev.*, 2014, **15**(11), 4377–4384.

2 I. Oakley-Girvan and S. W. Davis, Breath Based Volatile Organic Compounds in the Detection of Breast, Lung, and Colorectal Cancers: A Systematic Review, *Cancer Biomarkers*, 2017, **21**(1), 29–39.

3 M. Mirzaei, O. Gülseren, M. Rafienia and A. Zare, Nanocarbon-Assisted Biosensor for Diagnosis of Exhaled Biomarkers of Lung Cancer: DFT Approach, *Eurasian Chem. Commun.*, 2021, **3**, 154–161.

4 G. Gregis, S. Schaefer, J.-B. Sanchez, V. Fierro, F. Berger, I. Bezverkhyy, G. Weber, J.-P. Bellat and A. Celzard, Characterization of Materials Toward Toluene Traces Detection for Air Quality Monitoring and Lung Cancer Diagnosis, *Mater. Chem. Phys.*, 2017, **192**, 374–382.

5 M. M. Ayad and N. L. Torad, Alcohol Vapours Sensor Based on Thin Polyaniline Salt Film and Quartz Crystal Microbalance, *Talanta*, 2009, **78**(4–5), 1280–1285.

6 Z. Luo, P. Rong, Z. Yang, J. Zhang, X. Zou and Q. Yu, Preparation and Application of Co-doped Zinc Oxide: A Review, *Molecules*, 2024, **29**(14), 3373.
7 P. Panigrahi, H. Vovusha, Y. Pal, H. Bae, H. Lee, T. Kaewmaraya, S. Nazir, M. J. A. Shiddiky and T. Hussain, Identification of Lung Cancer Biomarkers by Nanosensors Based on Titanium Carbide (Ti3C2T*x*) MXenes, *ACS Appl. Nano Mater.*, 2023, **6**(23), 22117–22127.
8 X. Zhou, Z. Xue, X. Chen, C. Huang, W. Bai, Z. Lu and T. Wang, Nanomaterial-Based Gas Sensors Used for Breath Diagnosis, *J. Mater. Chem. B*, 2020, **8**(16), 3231–3248.
9 F. Villalpando-Páez, A. H. Romero, E. Muñoz-Sandoval, L. M. Martinez, H. Terrones and M. Terrones, Fabrication of Vapor and Gas Sensors Using Films of Aligned CNx Nanotubes, *Chem. Phys. Lett.*, 2004, **386**(1–3), 137–143.
10 F. Karlický, E. Otyepková, P. Banáš, P. Lazar, M. Kocman and M. Otyepka, Interplay Between Ethanol Adsorption to High-Energy Sites and Clustering on Graphene and Graphite Alters the Measured Isosteric Adsorption Enthalpies, *J. Phys. Chem. C*, 2015, **119**(35), 20535–20543.
11 A. Aasi, S. M. Aghaei and B. Panchapakesan, A Density Functional Theory Study on the Interaction of Toluene with Transition Metal Decorated Carbon Nanotubes: A Promising Platform for Early Detection of Lung Cancer from Human Breath, *Nanotechnology*, 2020, **31**(41), 415707.
12 A. Mosahebfard and M. Moaddeli, MoSe2 Nanosheet as a Lung Cancer Biosensor: A DFT Study, *J. Appl. Phys.*, 2023, **134**(11), 114501–114506.
13 S. Samanta, S. Kumar, V. R. Battula, A. Jaryal, N. Sardana and K. Kailasam, Quantum Dot-Sensitized O-Linked Heptazine Polymer Photocatalyst for the Metal-Free Visible Light Hydrogen Generation, *RSC Adv.*, 2020, **10**(50), 29633–29641.
14 D. Wang, W. Gu, Y. Zhang, Y. Hu, T. Zhang, X. Tao, W. Chen, *et al.*, Novel C-Rich Carbon Nitride for Room Temperature NO2 Gas Sensors, *RSC Adv.*, 2014, **4**, 18003–18006.
15 G. Dong, K. Zhao and L. Zhang, Carbon Self-Doping Induced High Electronic Conductivity and Photoreactivity of g-C_3N_4, *Chem. Commun.*, 2012, **48**(49), 6178–6180.
16 B. Zhu, L. Zhang, D. Xu, B. Cheng and J. Yu, Adsorption Investigation of CO2 on g-C_3N_4 Surface by DFT Calculation, *J. CO2 Util.*, 2017, **21**, 327–335.
17 P. Srinivasan, S. Samanta, A. Krishnakumar, J. B. B. Rayappan and K. Kailasam, Insights into g-C_3N_4as a Chemi-Resistive Gas Sensor for VOCs and Humidity-A Review of the State of the Art and Recent Advancements, *J. Mater. Chem. A*, 2021, **9**(17), 10612–10651.
18 J. Cao, Y. Gong, Y. Wang, B. Zhang, H. Zhang, G. Sun, H. Bala and Z. Zhang, Cocoon-Like ZnO Decorated Graphitic Carbon Nitride Nanocomposite: Hydrothermal Synthesis and Ethanol Gas Sensing Application, *Mater. Lett.*, 2017, **198**, 76–80.
19 D. Wang, S. Huang, H. Li, A. Chen, P. Wang, J. Yang, X. Wang and J. Yang, Ultrathin WO3 Nanosheets Modified by g-C_3N_4 for Highly Efficient Acetone Vapor Detection, *Sens. Actuators, B*, 2019, **282**, 961–971.
20 Y. Zhang, J. Liu, X. Chu, S. Liang and L. Kong, Preparation of g–C3N4–SnO2 Composites for Application as Acetic Acid Sensor, *J. Alloys Compd.*, 2020, **832**, 153355.
21 X. Li, Y. Wang, W. Tian and J. Cao, Graphitic Carbon Nitride Nanosheets Decorated Flower-Like NiO Composites for High-Performance Triethylamine Detection, *ACS Omega*, 2019, **4**(6), 9645–9653.
22 Y. Zhang, D. Zhang, W. Guo and S. Chen, The α-Fe 2 O 3/g-C 3 N 4 heterostructural nanocomposites with enhanced ethanol gas sensing performance, *J. Alloys Compd.*, 2016, **685**, 84–90.
23 Y. Gong, Y. Wang, G. Sun, T. Jia, L. Jia, F. Zhang, L. Lin, B. Zhang, J. Cao and Z. Zhang, Carbon Nitride Decorated Ball-Flower Like Co3O4 Hybrid Composite: Hydrothermal Synthesis and Ethanol Gas Sensing Application, *Nanomaterials*, 2018, **8**(3), 132.
24 X. Dong, K. Wu, W. Zhu, P. Wu, J. Hou, Z. Wang, R. Li, J. Wu, Z. Liu and X. Guo, TiO2 Nanotubes/g-C_3N_4 Quantum Dots/rGO Schottky Heterojunction Nanocomposites as Sensors for Ppb-Level Detection of NO2, *J. Mater. Sci.*, 2019, **54**(10), 7834–7849.
25 R. Zhang, Y. Wang, Z. Zhang and J. Cao, Highly Sensitive Acetone Gas Sensor Based on g-C_3N_4 Decorated MgFe2O4 Porous Microspheres Composites, *Sensors*, 2018, **18**(7), 2211.
26 C. Qin, Y. Wang, Y. Gong, Z. Zhang and J. Cao, CuO-ZnO hetero-junctions decorated graphitic carbon nitride hybrid nanocomposite: Hydrothermal synthesis and ethanol gas sensing application, *J. Alloys Compd.*, 2019, **770**, 972–980.
27 K. Sneha Mohanan and V. N. Dhilshada, Mausumi Chattopadhyaya, Density Functional Theoretical Method for Modelling Cobalt-Doped g-C3N4 Sensor for Detecting Acetone, Ethanol, and Aniline, *Cancer Biomarkers*, 2025, **10**(15), e202405976, DOI: 10.1002/slct.202405976.
28 V. N. Dhilshada, A. Chandran, S. Sen and M. Chattopadhyaya, Density Functional Theory-Based Modeling of the Half-Metallic g-C_3N_4/CoN_4 Heterojunction for Photocatalytic Water Splitting Reaction, *Phys. Chem. Chem. Phys.*, 2024, **26**, 21117–21133.
29 V. N. Dhilshada, S. Sen and M. Chattopadhyaya, Comparative Study of the Photocatalytic Activity of g-C_3N_4/MN4 (M = Mn, Fe, Co) for Water Splitting Reaction: A Theoretical Study, *J. Comput. Chem.*, 2024, **45**, 2518–2529, DOI: 10.1002/Jcc.27464.
30 V. N. Dhilshada, S. Sen and M. Chattopadhyaya, A Density Functional Study of Type I to Type II Crossover in g-C_3N_4/CoN_4 Heterostructure in Presence of External Perturbation, *Int. J. Hydrogen Energy*, 2024, **91**, 1136–1148.
31 V. N. Dhilshada and M. Chattopadhyaya, Theoretical Modeling of Direct Z-Scheme B,F-Doped g -C 3 N 4/CoN 4 Composites for Promoting Photocatalytic Water Splitting Reaction, *J. Phys. Chem. C*, 2025, **129**(11), 5625–5636.
32 P. Giannozzi, S. Baroni, N. Bonini, M. Calandra, R. Car, C. Cavazzoni, D. Ceresoli, G. L. Chiarotti, M. Cococcioni, I. Dabo, A. Dal Corso, S. de Gironcoli, S. Fabris, G. Fratesi, R. Gebauer, U. Gerstmann, C. Gougoussis, A. Kokalj, M. Lazzeri, L. Martin-Samos, N. Marzari, F. Mauri, R. Mazzarello, S. Paolini, A. Pasquarello, L. Paulatto,

C. Sbraccia, S. Scandolo, G. Sclauzero, A. P. Seitsonen, A. Smogunov, P. Umari and R. M. Wentzcovitch, QUANTUM ESPRESSO: A Modular and Open-Source Software Project for Quantum Simulations of Materials, *J. Phys.: Condens. Matter*, 2009, **21**, 395502.

33 J. P. Perdew, K. Burke and M. Ernzerhof, Generalized Gradient Approximation Made Simple, *Phys. Rev. Lett.*, 1996, **77**, 3865–3868.

34 A. Jain, G. Hautier, S. P. Ong, C. J. Moore, C. C. Fischer, K. A. Persson and G. Ceder, Formation Enthalpies by Mixing GGA and GGA + U Calculations, *Phys. Rev. B*, 2011, **84**, 045115.

35 S. Grimme, S. Ehrlich and L. Goerigk, Effect of the Damping Function in Dispersion Corrected Density Functional Theory, *J. Comput. Chem.*, 2011, **32**, 1456–1465.

36 H. J. Monkhorst and J. D. Pack, Special Points for Brillouin-Zone Integrations, *Phys. Rev. B*, 1976, **13**, 5188–5192.

37 G. Kresse and J. Furthmüller, Efficient Iterative Schemes Forab Initiototal-Energy Calculations Using a Plane-Wave Basis Set, *Phys. Rev. B*, 1996, **54**, 11169–11186.

38 E. Kroke, M. Schwarz, E. Horath-Bordon, P. Kroll, B. Noll and A. D. Norman, Tri-s-Triazine Derivatives. Part I. From Trichloro-Tri-s-Triazine to Graphitic C3N4 StructuresPart II: Alkalicyamelurates M3[C6N7O3], M = Li, Na, K, Rb, Cs, Manuscript in Preparation, *New J. Chem.*, 2002, **26**, 508–512.

39 F. Fina, S. K. Callear, G. M. Carins and J. T. Irvine, Structural Investigation of Graphitic Carbon Nitride via XRD and neutron Diffraction, *Chem. Mater.*, 2015, **27**(7), 2612–2618.

40 A. M. Silva and M. I. Rojas, Electric and Structural Properties of Polymeric Graphite Carbon Nitride (g-C_3N_4): A Density Functional Theory Study, *Comput. Theor. Chem.*, 2016, **1098**, 41–49.

41 D. Ghosh, G. Periyasamy, B. Pandey and S. K. Pati, Computational Studies on Magnetism and the Optical Properties of Transition Metal Embedded Graphitic Carbon Nitride Sheets, *J. Mater. Chem. C*, 2014, **2**, 7943–7951.

42 J. Deng, N. Liu, J. Guo and X. Chen, Large Spin Gaps in the Half-Metals M N 4 (M =Mn, Fe, Co) with N 2 Dimers, *Phys. Rev. B*, 2019, **99**, 184409.

43 F. Opoku, K. Kuben Govender, C. G. C. E. van Sittert and P. Poomani Govender, Charge Transport, Interfacial Interactions and Synergistic Mechanisms in BiNbO4/MWO4 (M = Zn and Cd) Heterostructures for Hydrogen Production: Insights from a DFT+U Study, *Phys. Chem. Chem. Phys.*, 2017, **19**, 28401–28413.

44 Y. Lin, Q. Wang, M. Ma, P. Li, V. Maheskumar, Z. Jiang and R. Zhang, Enhanced Optical Absorption and Photocatalytic Water Splitting of g-C_3N_4/TiO2 Heterostructure Through C&B Codoping: A Hybrid DFT Study, *Int. J. Hydrogen Energy*, 2021, **46**, 9417–9432.

45 S. Ebnesajjad, A. H. Landrock, *Surface Tension and its Measurement*, Elsevier eBooks, 2015, pp. 19–34.

46 M. E. Vaschetto, B. A. Retamal and A. P. Monkman, Density Functional Studies of Aniline and Substituted Anilines, *J. Mol. Struct.: THEOCHEM*, 1999, **468**(3), 209–221.

47 K. Tamagawa, T. Iijima and M. Kimura, Molecular Structure of Benzene, *J. Mol. Struct.*, 1976, **30**(2), 243–253.

48 E. G. Cox, Crystal Structure of Benzene, *Rev. Mod. Phys.*, 1958, **30**(1), 159–162.

49 R. B. David. and W. P. David., Toluene: Structure, Dynamics, and Barrier to Methyl Group Rotation in Its Electronically Excited State. A route to IVR, *J. Chem. Phys.*, 2000, **113**, 3658.

50 V. K. Bel'skii, L. A. Chetkina and V. A. Shuvaeva, Structure of o-toluidine (C14H16N2). repeated determination, *J. Struct. Chem.*, 1988, **28**(5), 803–805.

51 S. M. Aghaei, A. Aasi, S. Farhangdoust and B. Panchapakesan, Graphene-like BC6N Nanosheets Are Potential Candidates for Detection of Volatile Organic Compounds (VOCs) in Human Breath: A DFT Study, *Appl. Surf. Sci.*, 2021, **536**, 147756.

52 B. M. Yaseen, R. J. Albadr, V. Jain, A. Kumar, S. Ganesan, A. Shankhyan, S. Supriya, S. Ray, W. M. Taher, M. Alwan and M. J. Jawad, Modulating the Adsorption Properties of Benzene and Nitrobenzene Molecules on the Novel Ptn Cluster Modified C3N Nanosheets for Sensing Applications: A Comparative DFT Investigation, *J. Inorg. Organomet. Polym. Mater.*, 2025, **35**, 6005–6017.

53 A. Aasi, S. M. Aghaei and B. Panchapakesan, A density functional theory study on the interaction of toluene with transition metal decorated carbon nanotubes: a promising platform for early detection of lung cancer from human breath, *Nanotechnology*, 2020, **31**, 415707.

54 P. Panigrahi, H. Vovusha, Y. Pal, H. Bae, H. Lee, T. Kaewmaraya, S. Nazir, M. J. A. Shiddiky and T. Hussain, Identification of Lung Cancer Biomarkers by Nanosensors Based on Titanium Carbide (Ti3C2T_x) MXenes, *ACS Appl. Nano Mater.*, 2023, **6**(23), 22117–22127, DOI: 10.1021/acsanm.3c04313.

55 T. Liu, Z. Cui, X. Li, H. Cui and Y. Liu, Al-Doped MoSe2Monolayer as a Promising Biosensor for Exhaled Breath Analysis: A DFT Study, *ACS Omega*, 2021, **6**, 988–995.

56 L. Jiang, X. Yuan, G. Zeng, J. Liang, Z. Wu, H. Yu, D. Mo, H. Wang, Z. Xiao and C. Zhou, Nitrogen self-doped g-C3N4 nanosheets with tunable band structures for enhanced photocatalytic tetracycline degradation, *J. Colloid Interface Sci.*, 2019, **536**, 17–29.

57 J. Tauc, Optical Properties and Electronic Structure of Amorphous Ge and Si, *Mater. Res. Bull.*, 1968, **3**, 37–46.

58 M. S. Jyothi, V. Nagarajan and R. Chandiramouli, Interaction Studies of Benzene and Phenol on Novel 4–8 Arsenene Nanotubes – A DFT Insight, *Comput. Theor. Chem.*, 2021, **1204**, 113381.

59 V. B. T. Phung, T. N. Tran, Q. H. Tran, T. T. Luong and V. A. Dinh, Graphene as a Sensor for Lung Cancer: Insights into Adsorption of VOCs Using vdW DFT, *ACS Omega*, 2024, **9**(2), 2302–2313, DOI: 10.1021/acsomega.3c06159.

60 Y.-H. Zhang, C.-N. Wang, F.-L. Gong, P. Wang, U. Guharoy, C. Yang, H.-L. Zhang, S.-M. Fang and J. Liu, Ultrathin Agaric-Like ZnO with Pd Dopant for Aniline Sensor and DFT Investigation, *J. Hazard. Mater.*, 2020, **388**, 122069.

61 Q. Wan, Y. Xu and H. Xiao, Exhaled Gas Detection by Ir-Doped CNT for Primary Diagnosis of Lung Cancer, *AIP Adv.*, 2018, **8**(10), 105128, DOI: 10.1063/1.5050435.

62 T. Jiang, F. Nan, J. Zhou, F. Zheng, Y. Weng, T.-Y. Cai, S. Ju, B. Xu and L. Fang, Enhanced Photocatalytic and Photoelectrochemical Performance of g-C_3N_4/BiVO4 Heterojunction: A Combined Experimental and Theoretical Study, *AIP Adv.*, 2019, **9**(5), 055225.
63 V. Nagarajan and R. Chandiramouli, Twisted Bilayer Arsenene Sheets as a Chemical Sensor for Toluene and M-Xylene Vapours – A DFT Investigation, *J. Mol. Graphics Modell.*, 2021, **109**, 108034.
64 A. U. Rahman, D. M. Saaduzzaman, S. M. Hasan, *et al.*, Aluminum-Derived Nanotubes for Lung Cancer Detection: A DFT Inquisition, *Sci. Rep.*, 2025, **15**, 34852.